

Dear Author,

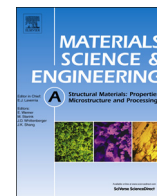
Please, note that changes made to the HTML content will be added to the article before publication, but are not reflected in this PDF.

Note also that this file should not be used for submitting corrections.



Contents lists available at ScienceDirect

## Materials Science &amp; Engineering A

journal homepage: [www.elsevier.com/locate/msea](http://www.elsevier.com/locate/msea)

# The effect of thermo-mechanical treatment on the high temperature tensile behavior of an alumina-forming austenitic steel

Bin Hu, Ian Baker\*

Thayer School of Engineering, Dartmouth College, Hanover, NH 03755, USA

## ARTICLE INFO

## Article history:

Received 23 September 2015

Received in revised form

11 November 2015

Accepted 12 November 2015

## Keywords:

Alumina-forming austenitic steel

Strain rate sensitivity

Activation volume

Strain rate jump tests

Deformation mechanism

Dynamic strain aging

## ABSTRACT

Two different thermo-mechanical treatments (TMT) were performed on an alumina-forming austenitic (AFA) stainless steel, DAFA 29, which was recently developed at Oak Ridge National Laboratory for application in advanced ultra-supercritical power plants. The resulting fine-grained TMT materials showed yield stresses more than double the yield stress of the as-received material at room temperature and more than 50% higher at 600 °C, but lower yield stresses (but greater elongations) at 700 °C and above. Strain rate jump tests performed at both 600 °C and 700 °C showed that the TMT materials have greater strain rate sensitivity and lower activation volumes at both temperatures. The strain rate has a power law relationship with the flow stress with a stress exponent of ~5. The as-received AFA alloy showed serrated stress-strain curves at 600 °C suggesting the occurrence of dynamic strain aging.

© 2015 Published by Elsevier B.V.

## 1. Background

An effective way to enhance the energy conversion efficiency and reduce the carbon footprint of fossil fuel power plants is to increase their operating temperature and pressure. The operating temperature and pressure of current ultra-supercritical (USC) power plants are 600 °C/25 MPa which will eventually increase to 700 °C/35 MPa and then later to 760 °C/35 MPa for the next generation of advanced ultra-supercritical (A-USC) power plants [1–4]. The materials used for boiler/steam turbine in the A-USC power plant must be able to withstand not only this high operating temperature, but also excellent oxidation and corrosion resistance, most importantly at low cost [4,5]. This latter requirement is problematic for nickel and titanium alloys which are expensive.

Heat-resistant FeNi-based austenitic stainless steels could potentially be used for USC power plants due to their good creep, good oxidation resistance and relatively low cost. However, they rely on the formation of chromia ( $\text{Cr}_2\text{O}_3$ ) as the surface protection layer and this starts to lose its protective capability under aggressive environments at temperature above ~650 °C [6–8]. One potential solution is the development of alumina-forming austenitic (AFA) stainless steels. AFA stainless steels can form alumina scale on the material's surface. This alumina scale is more thermodynamically stable, grows slower than chromia ( $\text{Cr}_2\text{O}_3$ ), and it

can provide better oxidation resistance than conventional heat resistant stainless steels in many harsh environments [5,8–12].

Recently-developed AFA stainless steels exhibit the promising mechanical properties and oxidation resistance [8–14]. These AFA alloys fall in the composition ranges Fe–(12–35)Ni–(12–15)Cr–(2.5–4)Al–(0.6–3)Nb (wt%) with additions of Nb, Ti, Si, C, and B to improve the creep and oxidative properties [8]. They have a single phase austenitic microstructure with MC carbide and/or  $\text{L}_{12}$ -Ni<sub>3</sub>(Al, Ti) as the main strengthening precipitates [11,12]. The Laves phase on the grain boundaries also play an important strengthening role [13,14]. Among these alloys, Fe–14Cr–32Ni–3Nb–3Al–2Ti (wt%), recently developed by Oak Ridge National Laboratory (ORNL) and referred as DAFA29, with various minor elemental additions shows the best creep performance [12].

In a previous study, two TMTs were performed on DAFA29 in an attempt to further improve its mechanical properties. The microstructures and deformation behavior of this AFA alloy in both the as-received condition and after the TMTs were characterized at room temperature. The TMTs reduced the grain size significantly to the nanoscale (~100 nm) and increased the room temperature yield strength to above 1000 MPa [15].

In this paper, the deformation behavior of this AFA alloy in both the as-received condition and after the TMTs was studied at elevated temperatures. The flow stress of the TMT materials was evaluated at different strain rates, and the high temperature deformation mechanisms were characterized.

\* Corresponding author.

E-mail address: [Ian.Baker@dartmouth.edu](mailto:Ian.Baker@dartmouth.edu) (I. Baker).

## 2. Experiment

### 2.1. Materials preparation

The DAFA29 used in this study was obtained from ORNL (Oak Ridge, TN). Ingots of the alloys had been hot-rolled at 1100 °C (80% thickness reduction with ~15–20% thickness reduction per pass) and then annealed at 1100 °C for 30 min in Ar+4% H<sub>2</sub> gas, followed by air-cooling. The chemical composition of this alloy, as analyzed using inductively coupled plasma spectroscopy and gas combustion techniques at ORNL, is shown in Table 1.

Two TMTs of the DAFA29 were performed in an attempt to produce finer and uniformly distributed precipitates [15]. In the first approach (referred to as Method #1), the DAFA29 was cold rolled to a 90% reduction in thickness with a ~4.5% reduction per pass, and then annealed at 800 °C for 2.4, 24, or 240 h. The grain sizes of the thermomechanically treated alloys ranged from ~100 nm to ~1 μm depending on different annealing time. In the second approach (referred to as Method #2), the alloy was given a solutionizing anneal at 1200 °C and then cold rolled to a 90 % reduction in thickness with a ~4.5% reduction per pass before annealing at 800 °C for 2.4, 24, or 240 h. As the annealing time was increased from 2.4 to 240 h, the grain size increased from ~200 nm to ~2 μm. The as-received DAFA29 has a grain size of ~40 μm with niobium enriched precipitates (~10 μm) randomly distributed in the matrix and grain boundaries. After TMT, finer and uniformly distributed precipitates (~560 nm) are present. Details of the microstructures of these thermo-mechanical treatments were described in a previous paper [15].

### 2.2. Mechanical testing

Tensile test specimens were milled to dog-bone geometry with a gauge length of 10 mm, width of 2.65 mm, thickness of 0.8 mm, and polished to a mirror finish using 800 grit silicon carbide papers followed by 0.3 μm alumina powder.

Elevated temperature (600 °C, 700 °C and 800 °C) tensile tests were performed with an Instron 5690 tensile testing machine and a MTS hydraulic testing machine. A preload force of 50 N was applied before the tensile tests. The initial strain rate for all tensile tests was  $5 \times 10^{-4} \text{ s}^{-1}$ . Elongations were measured directly from the gauge of the specimens after the tensile tests. All the tensile tests were performed three times for each specimen. The resulting test data are shown as true stress–true strain curves.

Strain rate jump tests were performed on the same tensile test machine at 600 °C and 700 °C. A preload force of 50 N was again

applied before the strain rate jump tests were started. The initial strain rate for all strain rate jump tests was  $5 \times 10^{-5} \text{ s}^{-1}$ .

### 2.3. Microstructural analysis

For scanning electron microscope (SEM) analysis, samples were polished using increasingly fine grades of silicon carbide papers and then further polished using 0.3 μm alumina powders to obtain a mirror finish. The polished samples were polished with a vibrometer (Buehler, Lake Bluff, IL) for 3 h. The specimens were then examined in an FEI XL-30 field emission gun (FEG) SEM operated at 15 keV, using backscattered electron (BSE) image mode.

Thin foils for transmission electron microscope (TEM) examination were produced from 3 mm dia., 200 μm thick discs by twin-jet electropolishing at 9.5 V and ~100 mA in a solution of 25% nitric acid in methanol at –20 °C using a Struers Tenupol 5. The resulting thin foils were examined using an FEI Tecnai F20 FEG TEM operated at 200 kV and equipped with energy dispersive X-ray spectroscopy (EDS).

## 3. Results

### 3.1. Tensile tests at elevated temperatures

Tensile tests of TMT Method#1 alloys were performed at 700 °C. The stress strain curves of the three TMT alloys are shown in Fig. 1a. All three TMT alloys show lower yield strength but higher elongation compared to the as-received DAFA29, see Table 2. The tensile behaviors of these TMT alloys at 700 °C are significantly different from room temperature. They show yield strength above 1000 MPa in room temperature tensile tests [15].

Tensile tests of TMT alloys Method#2 were also carried out at 700 °C. The stress strain curves of the three TMT alloys are shown in Fig. 1b. The results are similar to the stress strain curves observed for the TMT Method#1 tests. All the TMT alloys show lower yield strength, but higher elongation. The yield strengths (measured as 0.2% proof stress) were in the range of 270–346 MPa, see Table 2.

After the tensile tests at 700 °C, all test specimens were characterized using the SEM. All the treated samples have different shapes of the necked region because of differences in ductility. TMT (Method#1) alloys after ageing for 2.4 h, 24 h and 240 h showed reductions in area of 33%, 64%, and 93%, respectively. The differences in the reduction in area are due to the different grain sizes for these three treated samples [15]. The grain sizes of TMT (Method#1) annealed for 2.4 h, 24 h and 240 h samples are ~100 nm, ~270 nm, and ~1 μm, respectively [15]. Thus, the elongation and reduction in area increased with increasing grain size, presumably due to the reduction in yield strength.

For TMT alloys treated using Method#2, the reductions in area for the 2.4 h, 24 h and 240 h samples were 49%, 67% and 91%, respectively. The microstructures of these TMT alloys were shown in our previous work in [15]. The grain size of TMT samples with ageing 2.4 h, 24 h and 240 h are ~200 nm, ~450 nm, and ~2 μm, respectively. The 240 h annealed TMT alloy also has the largest area reduction and the highest elongation up to 53% due to the grain growth to larger than 2 μm during 800 °C annealing [15].

Fig. 2 shows fracture surfaces of as-received DAFA29, TMT 2.4 h, 24 h and 240 h samples after tensile testing at 700 °C. The fracture surface of as-received DAFA29 shows ductile failure with large ductile dimples and considerable plastic deformation between the dimples. The fracture surfaces of TMT alloys are covered with a thick layer of oxide due to exposure at high temperature during the tensile tests. However, the Laves phase precipitates, which show white contrast, are still visible. There are no dimples evident

**Table 1**  
Analyzed chemistry (wt%) of as-received DAFA29 [15].

Element	wt%
Fe	45.34
Cr	13.83
Mn	0.13
Ni	32
Cu	0.12
Al	3.02
Si	0.15
Nb	2.87
V	< 0.01
Ti	2
Mo	0.1
W	< 0.01
Zr	0.32
C	0.11
B	0.0085
P	< 0.005
N	< 0.0001

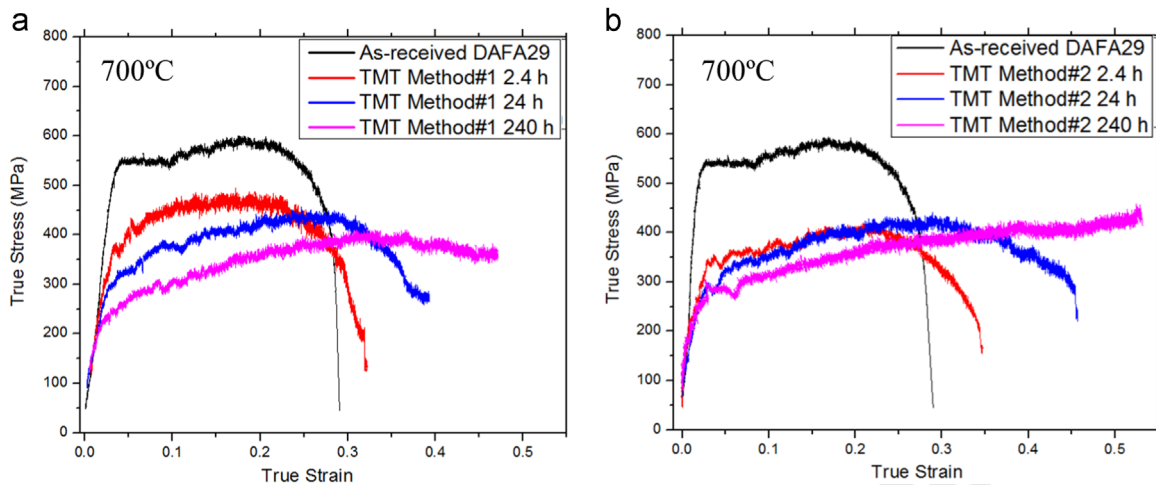


Fig. 1. Stress strain curves of as-received and TMT DAFA29 at 700 °C, (a) after TMT Method#1, (b) after TMT Method#2.

on the fracture surface for all three TMT alloys, although the materials are all much more ductile than as-received DAFA29. This ductility is due to the small grain sizes (ranging from  $\sim 100$  nm to  $1\ \mu\text{m}$ ) of these three TMT samples. All three fracture surfaces are covered by a layer of oxide formed during tensile test at 700 °C

As-received and TMT DAFA29 samples were also tested at elevated temperatures from 600 °C to 800 °C. The resulting true stress-strain curves are shown in Fig. 3. At 600 °C (Fig. 3a), the stress strain curve of as-received DAFA29 has a yield stress of 535 MPa, shows considerable work-hardening and an ultimate tensile strength of 665 MPa at an elongation of 20%. The TMT alloys showed higher yield strengths of 928 and 886 MPa for Method#1 and Method#2, respectively. At 800 °C, the yield strength of as-received DAFA29 decreased to 360 MPa with no work-hardening evident. The yield strength of TMT alloys decreased dramatically lower to 150 (Method#1) and 120 MPa (Method#2) with elongations more than 40%.

Fig. 4 provides a summary of the yield stress of as-received and TMT DAFA29 tested at different temperatures. The behavior of as-received DAFA29 is similar to many f.c.c. alloys reported in the literature [3,16], i.e.: nickel-base superalloys and nickel iron-base superalloy. The yield strength is not greatly affected by the increase in temperature until it reaches a certain temperature. This transition temperature is 600 °C for the as-received DAFA29. The flow stress of  $\text{L}_{12}$  precipitates increase anomalously with increase of temperature. Therefore, the temperature independence of the yield strength of AFA alloys until 600 °C is the net effect of strength reduction of f.c.c. phase compensated by the increase of strength from  $\text{L}_{12}$  precipitates [17].

The TMT AFA alloys show yield stresses significantly larger than the as-received DAFA29 at room temperature. This is due to the fine grain size present after the TMT process for both TMT methods (100–200 nm). Details of the room temperature tensile test results were described in previous paper [15]. As the temperature increased to 600 °C, the yield stress of the TMT alloys decreased

gradually until 600 °C and then decreased dramatically at 700 °C. This significant loss of stress in the range of 600–700 °C might be due to increased diffusion rates in TMT alloys leading to fast dislocation climb. The large volume of grain boundaries in TMT alloys lose the function to interrupt of dislocation motion due to the fast dislocation climbing. The grain boundaries work as sites of weakness at above 600 °C.

At 800 °C, this grain boundary effect is more obvious. The yield strength of TMT alloys is less than half of the yield strength of as-received DAFA29 as shown in Fig. 4. At this temperature, dislocations will be able to move around obstacles easily, the grain refined TMT alloys become significantly weaker.

### 3.2. Strain rate jump tests at elevated temperatures

Generally, the flow stress of alloys at elevated temperature is a function of the applied strain rate. The magnitude of the effect is expressed by the strain rate sensitivity  $m$ . Theoretically, it is possible to carry out a series tensile tests at various temperatures and strain rates. In practice, this is rarely done because of the limitations of time and the numbers of specimens required. Instead, strain rate jump tests can be performed using a single specimen. The strain rate is increased to a second level (approximately an order of magnitude) once a steady state flow stress is obtained.

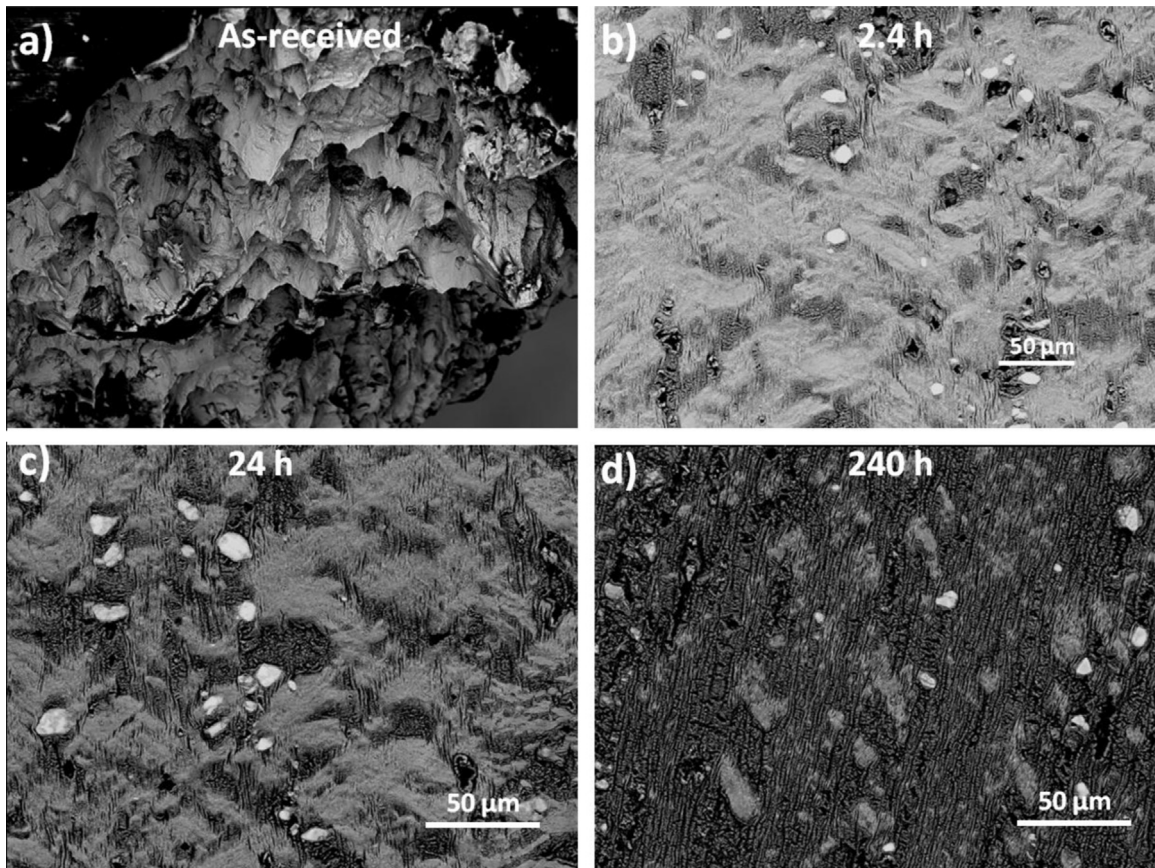
Strain rate jump experiments were performed on as-received and TMT DAFA29 at 600 °C. The strain rate jump test results are shown in Fig. 5a. The initial strain rate was  $5 \times 10^{-5}\ \text{s}^{-1}$  with an order of magnitude increase for each jump. The flow stresses of both TMT alloys increased with the strain rate increases. But, the flow stress of as-received DAFA29 is relatively independent of strain rate at this temperature. It is insensitive to the strain rate change at 600 °C. It is worth noting the serrations that occurred on the as-received DAFA29 during testing at 600 °C. The serrated flow starts when the strain rate jumps from  $5 \times 10^{-5}\ \text{s}^{-1}$  to  $5 \times 10^{-4}\ \text{s}^{-1}$ . It is thought to be related to dynamic strain aging in

Table 2

Yield strength, elongation at fracture, and reduction in area at the neck for the as-received and TMT DAFA29 after tensile tested at 700 °C

Materials	TMT Method#1			TMT Method#2		
	Yield strength (MPa)	Elongation (%)	Reduction in area (%)	Yield strength (MPa)	Elongation (%)	Reduction in area (%)
As-received	523	28	30	523	28	30
TMT 2.4 h	393	32	33	346	33	49
TMT 24 h	298	38	64	298	45	67
TMT 240 h	225	46	93	270	53	91





**Fig. 2.** BSE images of fracture surfaces for as-received (a) and TMT DAFA29 (Method#1, (b) is for 2.4 h, (c) is for 24 h and (d) is for 240 h) tensile tested at 700 °C annealed for the times indicated.

this material. We will further explain these serrations in the discussion section.

Strain rate jump tests were also performed at 700 °C which is the target application temperature for AFA stainless steels. The results of strain rate jump tests of as-received and TMT DAFA29 performed are shown in Fig. 5b. The initial strain rate was  $5 \times 10^{-5} \text{ s}^{-1}$  with an order of magnitude increase for each jump. The flow stresses of all samples increased with the strain rate increasing. At the strain rate of  $5 \times 10^{-5} \text{ s}^{-1}$ , the flow stress of as-received DAFA29 was 445 MPa which is almost twice that of TMT DAFA29 of 292 MPa. When the strain rate is jumped to

$5 \times 10^{-2} \text{ s}^{-1}$ , the flow stress of as-received DAFA29 was 829 MPa, which is less than that of TMT DAFA29 of 1080 MPa.

### 3.3. Strain rate influence on microstructures

In order to understand the fracture behavior of as-received DAFA29 at different strain rates, tensile tests of as-received DAFA29 alloys were performed at 700 °C for selected strain rates ( $5 \times 10^{-6} \text{ s}^{-1}$ ,  $5 \times 10^{-4} \text{ s}^{-1}$ , and  $5 \times 10^{-2} \text{ s}^{-1}$ ). The resulting true stress–strain curves are shown in Fig. 6. The flow stresses are comparable to the results from the strain rate jump test results

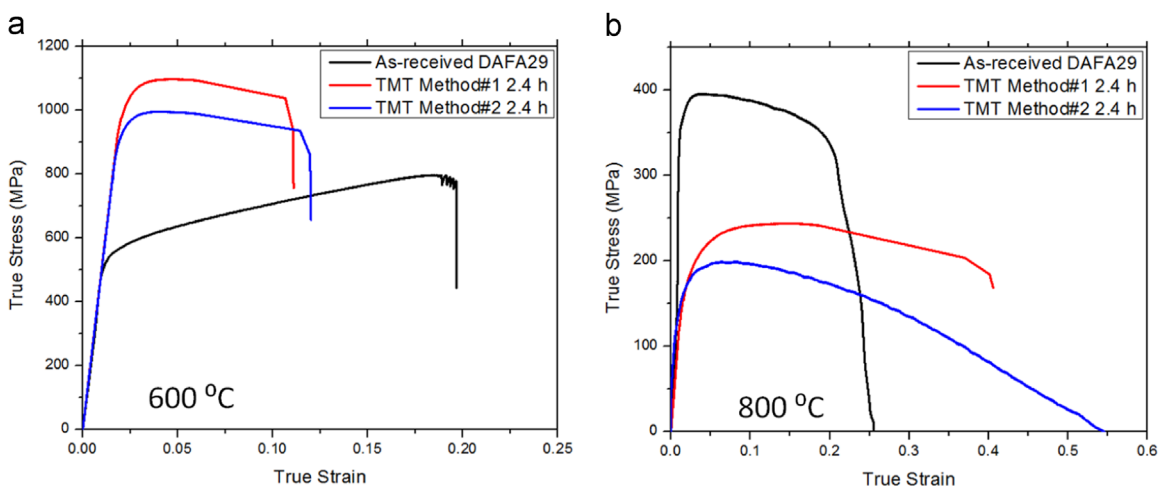


**Fig. 3.** True stress–strain curves for as-received and TMT DAFA29 at 600 °C (a) and 800 °C (b). All the tensile tests were performed with an initial strain rate of  $5 \times 10^{-4} \text{ s}^{-1}$ .

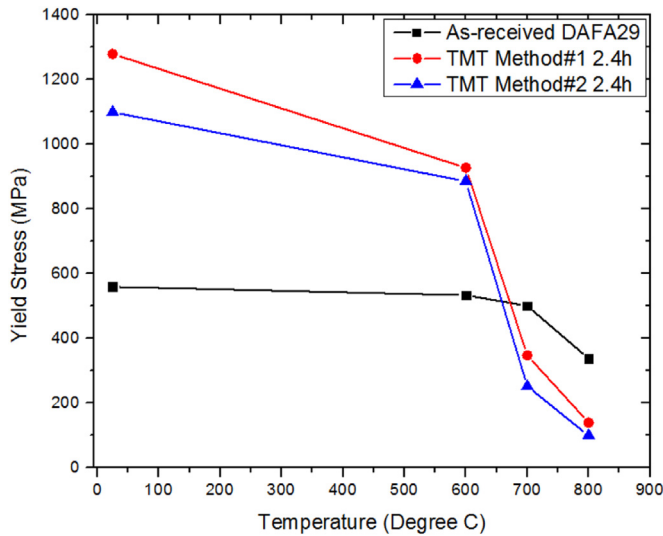


**Fig. 4.** Yield stress of as-received DAFA29 and TMT DAFA29 (Method#1 and Method#2) as a function of temperatures (All the tests were performed at strain rate of  $5 \times 10^{-4} \text{ s}^{-1}$ ).

shown in Fig. 5. Both the yield strength and work-hardening rate increase with increasing strain rate. A summary of the yield strengths and work-hardening rates is shown in Table 3.

TEM observations were used in order to investigate the dislocation distributions at 700 °C. Fig. 7 shows bright field (BF) TEM images for the samples tested at different strain rates. The sample (Fig. 7a) tested at  $5 \times 10^{-2} \text{ s}^{-1}$  has the highest dislocation density compared to the other two samples. The high dislocation density in Fig. 7a effectively enhanced the dislocation interactions which created additional barriers in the lattice for slip. These barriers produced the high work hardening rate observed at this strain rate (Fig. 6). For the lower strain rates, the dislocation density was also lower. The samples tested at both  $5 \times 10^{-4}$  and  $5 \times 10^{-6} \text{ s}^{-1}$  show no work hardening and lower dislocation densities. The dislocations in Fig. 7a are observed to align along one direction. This might be due to the high strain rate during the tensile test.

In Fig. 7c,  $\text{Fe}_2\text{Nb}$  Laves phase and  $\text{NiAl}$  precipitates are present. These precipitates are located on grain boundaries and they are generated during the low strain rate test. Small ( $\sim 26 \text{ nm}$ ) spherical  $\text{L}_{12}\text{-Ni}_3(\text{Al,Ti})$  precipitates are also uniformly distributed in the f.c.c. matrix. The dislocations show strong interactions with these  $\text{L}_{12}$  precipitates. Numerous dislocation loops around  $\text{L}_{12}$

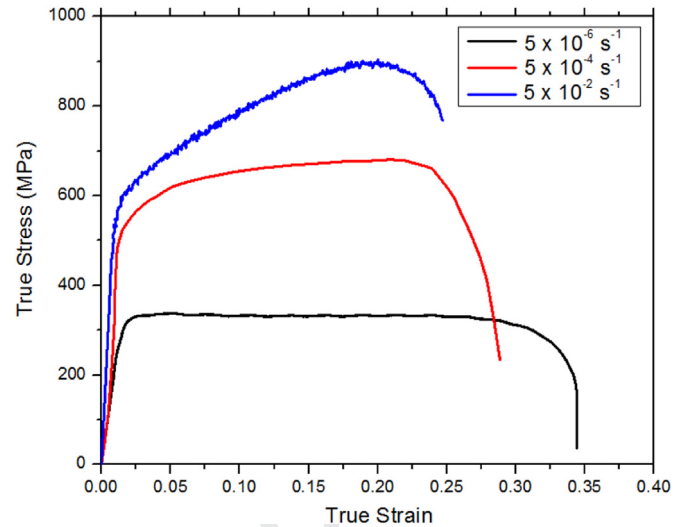


**Fig. 6.** True stress–strain curves for as-received DAFA29 at different strain rates at 700 °C.

**Table 3**

Yield strength and work-hardening rate of as-received DAFA29 at different strain rates.

Strain rate ( $\text{s}^{-1}$ )	Yield strength (MPa)	Work-hardening rate $n$
$5 \times 10^{-6}$	280	0
$5 \times 10^{-4}$	560	0.10
$5 \times 10^{-2}$	580	0.19

precipitates are present. The pinning effects of the precipitates result in the observed wavy dislocations. On the grain boundaries, numerous dislocations are crowded around the  $\text{Fe}_2\text{Nb}$  Laves phase suggesting that the Laves phase precipitates are very strong obstacles to dislocation motion.

#### 4. Discussion

At 700 °C, the yield strength of as-received DAFA29 is 523MPa and it is slightly lower than its room temperature yield strength 560 MPa [15]. It work-hardens significantly with an elongation of 20% at room temperature, while it shows low work-hardening rate at 700 °C with an elongation of 28%.

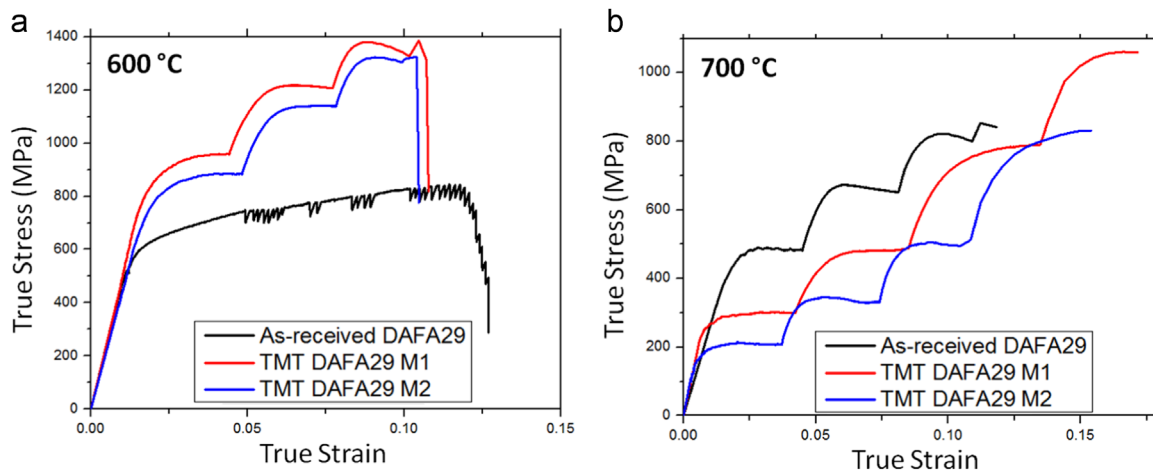


**Fig. 5.** Strain rate jump tests of as-received and TMT DAFA29 (Method#1 and Method#2) at 600 °C (a) and 700 °C (b). Each strain rate jump is increased by an order of magnitude starting at an initial strain rate of  $5 \times 10^{-5} \text{ s}^{-1}$ .



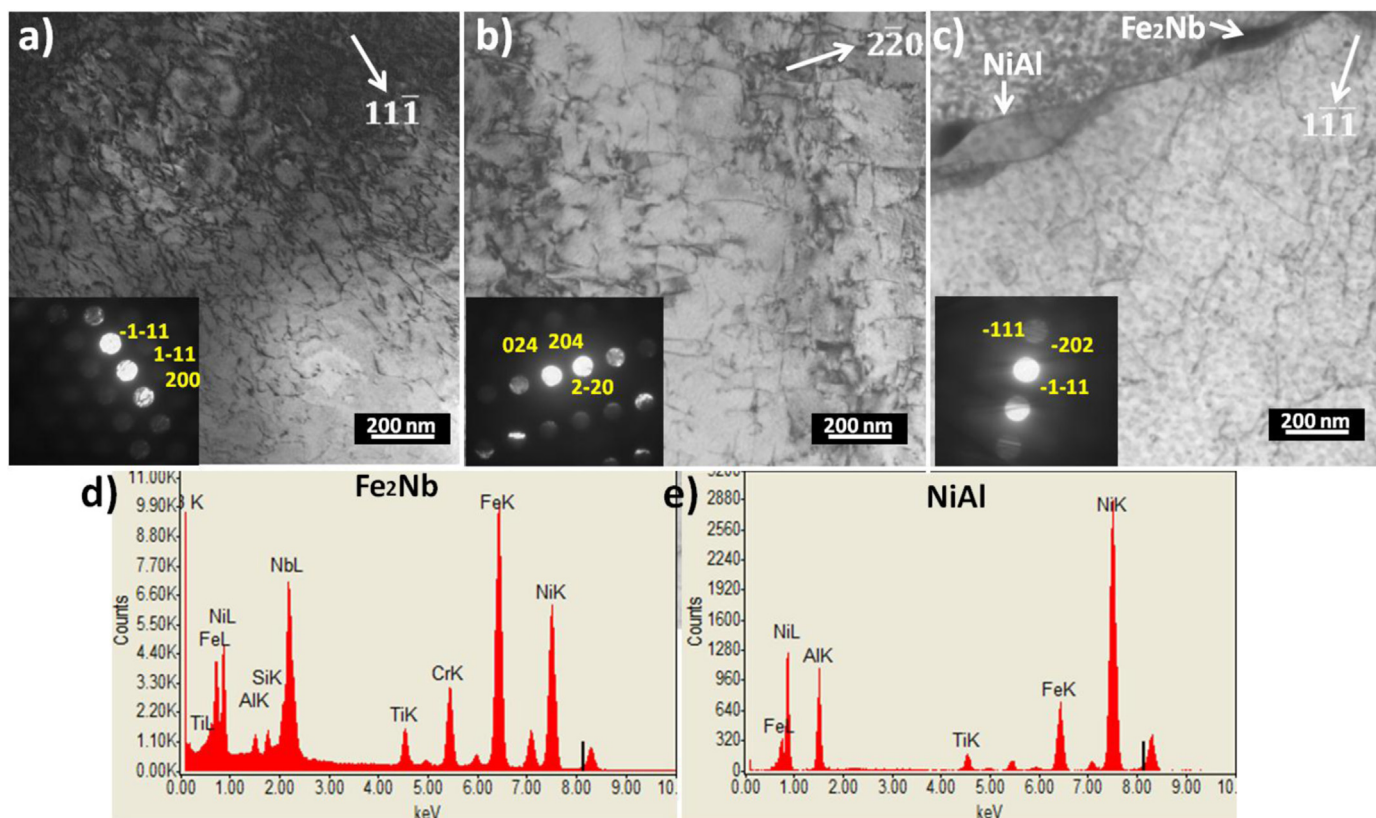


**Fig. 7.** BF TEM images of dislocations in DAFA29 after 700 °C tensile tests at different strain rates: (a)  $5 \times 10^{-2} \text{ s}^{-1}$ , (b)  $5 \times 10^{-4} \text{ s}^{-1}$ , (b)  $5 \times 10^{-6} \text{ s}^{-1}$ . (d) and (e) show EDS results from the grain boundary precipitates of Fe<sub>2</sub>Nb and NiAl for the sample tested at strain rate of  $5 \times 10^{-6} \text{ s}^{-1}$ .

**Table 4**

Summary of flow stress at different strain rate for the as-received and TMT DAFA29 at 600 °C and 700 °C.

Strain rate ( $\text{s}^{-1}$ )	Flow stress (MPa)					
	600 °C			700 °C		
	DAFA29	Method#1 2.4 h	Method#2 2.4 h	DAFA29	Method#1 2.4 h	Method#2 2.4 h
$5 \times 10^{-6}$	742	958	885	341	301	214
$5 \times 10^{-4}$	792	1216	1138	489	482	346
$5 \times 10^{-3}$	828	1375	1322	673	789	505
$5 \times 10^{-2}$				822	1061	831

The TMT alloys show lower yield strength ( $\sim 390$  MPa) but higher elongation compared to the as-received DAFA29, see Figs. 1 and 4. It is evident that the TMTs which result in a fine grain size significantly improve the room temperature properties, but this grain size strengthening is negligible at 700 °C. In room temperature, assuming off-set stress  $\sigma_0$  is constant for all TMT alloys, the estimate grain size strengthening effect is  $\sim 600$  MPa according to the  $\Delta\sigma = Kd^{-1/2}$  [15,18].

As the temperature increased to 700 °C, the strengthening effect becomes negligible due to the weakness of grain boundaries. For the 2.4 h annealed samples, the TMT Method #1 alloy still showed higher strength than TMT Method #2 alloy at 700 °C although it has more grain boundaries (smaller grain size). This is mainly because the high temperature strength of TMT alloys has a strengthening contribution from the small Laves phase precipitates as well as the grain boundaries. The Laves phase precipitates in TMT Method #1 alloys are in the range of  $167 \pm 37$  nm which is slightly smaller than it is in TMT Method #2 alloys ( $175 \pm 45$  nm) [15].

For all the annealed specimens, the 2.4 h and 24 h annealed TMT Method#1 alloys shows higher yield strength compared to

TMT Method#2 alloys due to a smaller grain size. When the annealing time was increased to 240 h, TMT Method#2 alloys have higher strength than TMT Method#2. This might be due to an increase in the volume fraction of the Laves phase during the long time aging process. After 240 h aging, the large Laves phase precipitates in TMT Method#2 alloys are not present. Instead smaller Laves phase are precipitated out with size of  $\sim 560$  nm [15]. In TMT Method#1 alloys, there are still large Laves phase precipitate present in the microstructure.

The following section will discuss the strain rate sensitivity of the as-received and TMT DAFA29. The deformation mechanism at elevated temperature will also be discussed based on the flow stress and strain rate for each alloy. Table 4 summarizes the flow stress at different strain rates for the as-received and TMT DAFA29 alloys.

#### 4.1. Strain rate sensitivity

The flow stress and strain rate are typically related at a constant elevated temperature by the following equation:

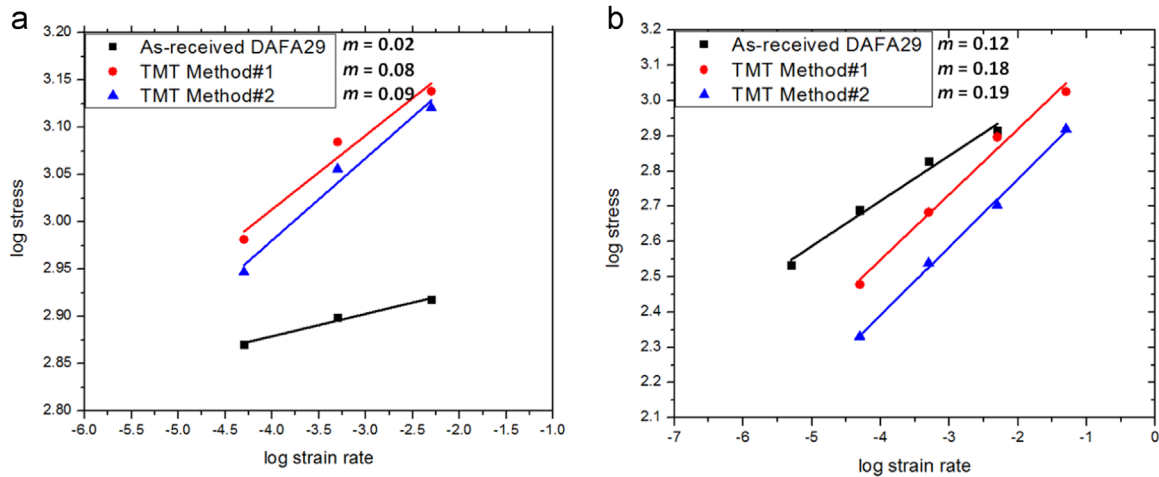


Fig. 8. Stress as a function of strain on log-log scale plots from data obtained for alloys tested at (a) 600 °C and (b) 700 °C.

$$\sigma = C\dot{\epsilon}^m \quad (1)$$

where  $C$  is a constant,  $\sigma$  is the flow stress,  $\dot{\epsilon}$  is the strain rate, and  $m$  is the strain rate sensitivity parameter.

Based on the flow stress results shown in Table 4, the flow stress is plotted as a function of strain rate on a log-log scale in Fig. 8. The strain rate sensitivity  $m$  can be obtained from

$$m = \frac{\log(\sigma)}{\log(\dot{\epsilon})} \quad (2)$$

The  $m$  value can be obtained based on a linear fit as shown in Fig. 8.  $m$  of as-received DAFA29 is 0.12, while the values for TMT DAFA29 is 0.18 (Method#1) and 0.19 (Method#2), i.e. the yield stresses of the TMT DAFA29 alloys are more sensitive to strain rate compared to the as-received DAFA29 at 700 °C. The slight difference in  $m$  values for TMT Method#1 and Method#2 is probably due to different grain sizes [15]. At 600 °C  $m$  for as-received DAFA29 is 0.02, whereas the  $m$  values for the TMT AFA alloys are 0.08 (Method#1) and 0.09 (Method#2). All the  $m$  values obtained at 600 °C are much smaller than those obtained at 700 °C, indicating that the strain rate sensitivity is influenced by the temperature for all tested alloys.

At both 600 °C and 700 °C, the alloys treated by Method#2 with a grain size of  $\sim 200$  nm have a slightly higher  $m$  than alloys treated by Method#1. Alloys treated by Method#1 have a grain size of  $\sim 100$  nm which is about half size of alloys treated by Method#2. It shows an increase in strain rate sensitivity with decreasing grain size. This trend has also been observed in other nanocrystalline alloys [19,20].

At the same testing temperature, the strain rate sensitivity is larger for the smaller nano-sized grains in the TMT alloys compared to coarse grains of  $\sim 40 \mu\text{m}$  for the as-received DAFA29. A number of models [19,21,22] indicate a grain size dependence of the strain rate sensitivity is related to a decrease in the activation volume  $V$ .

The strain rate sensitivity  $m$  can also be expressed as [20,21,23]:

$$m = \frac{\sqrt{3}kT}{V\sigma} \quad (3)$$

where  $k$ ,  $T$ ,  $V$  and  $\sigma$  are Boltzman constant, absolute temperature, activation volume and yield/flow stress, respectively. The activation volume  $V$  is directly related to the physical mechanisms of plastic deformation.

The activation volume  $V$  can be calculated based on Eqs. (2) and (3). A plot of  $\log(\dot{\epsilon})/\log(\sigma)$  as function of  $\sigma$  has a slope of  $V/\sqrt{3}kT$

and activation volumes can be obtained based on the value of the slope. The activation volume for metals is normally expressed in terms of  $b^3$ , where  $b$  is the shortest burgers vector of a perfect dislocation. In f.c.c. iron the Burgers vector is 0.253 nm [24]. The calculated activation volumes for DAFA29 at 700 °C is  $1.1 b^3$ , while the values for the TMT alloys are  $0.7 b^3$  (Method#1) and  $0.8 b^3$  (Method#2) respectively. The activation volume for the fine grained TMT alloys is smaller than that of the coarse-grained alloys. Dislocations have a higher activation barrier when the grain size enters the nanometer regime. This is similar to other alloys tested at both room temperature and elevated temperature [24–26].

#### 4.2. Deformation mechanisms

The relationship between strain rate and stress of the precipitation-strengthened alloys at elevated temperature can be described by a power law [7,27]:

$$\dot{\epsilon} = A \left( \frac{GbD}{kT} \right) \left( \frac{\sigma}{G} \right)^n \quad (4)$$

where  $G$  is shear modulus,  $b$  is Burgers vector,  $D$  is diffusion coefficient of the f.c.c. matrix,  $k$  is the Boltzmann constant,  $T$  is absolute temperature, and  $n$  is the stress exponent. A stress exponent  $n$  in the range of 3–5 is typical for solid solution alloys. Specifically,  $n$  is 5 for nickel and nickel-chromium alloys [27–29]. For precipitate-strengthened alloys, the  $n$  values obtained are normally larger than the solid solution alloys [30]. The high stress exponent arising from small dispersed precipitates being obstacles to the movement of dislocations [31,32].

In order to reduce the high stress exponent values, a threshold stress term  $\sigma_t$  is introduced into Eq. (4) to account for the influence of the precipitates. The effective stress is defined as  $\sigma - \sigma_t$ . Thus, Eq. (4) can be rewritten as:

$$\dot{\epsilon} = A' \left( \frac{GbD}{kT} \right) \left( \frac{\sigma - \sigma_t}{G} \right)^n \quad (5)$$

The value of the threshold stress  $\sigma_t$  depends on the dislocation precipitate interaction mechanism. The mechanism could be dislocation cutting, Orowan looping, or dislocation climb. This value can be determined using the methodology suggested by Lagneborg and Bergman [33]. Basically, Eq. (5) can be rewritten:

$$\dot{\epsilon}^{1/n} = A'' (\sigma - \sigma_t) \quad (6)$$

The threshold stress  $\sigma_t$  can be obtained from a plot of  $\dot{\epsilon}^{1/n}$  as a



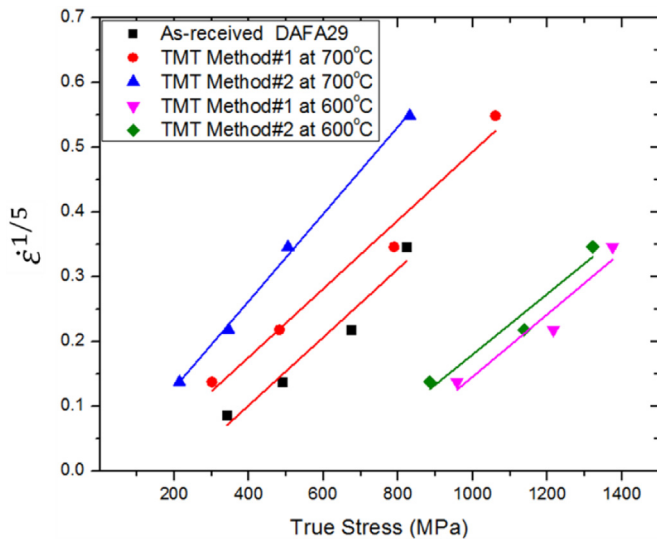


Fig. 9. Plots of  $\dot{\epsilon}^{1/5}$  as a function of stress for as-received DAFA29 and the TMT alloys.

function of  $\sigma$ , as shown in Fig. 9 and the threshold stress is the x-intercept. The threshold stress obtained using this method is 217 MPa for as-received DAFA29 at 700 °C, which is similar to the threshold stress value measured in another AFA alloy tested at the same temperature [7]. The threshold stresses are 50 MPa (Method#1) and 9 MPa (Method#2) for the TMT alloys tested at 700 °C. These values increase to 670 MPa (Method#1) and 574 MPa (Method#2) for the TMT alloys tested at 600 °C. Table 5 provides a summary of threshold stresses for the different processing conditions. The threshold stress of alloys treated by Method#1 is slightly larger than Method#2 for both temperatures. The value of the threshold stress decreased significantly with an increase in temperature, is almost zero for alloys treated by Method#2 at higher temperature.

Fig. 10 shows plot of strain rate as a function of effective stress ( $\sigma - \sigma_t$ ) for the as-received and TMT DAFA29 alloys. The corrected  $n$  value is 4.2 for the as-received DAFA29 tested at 700 °C which is close to the stress exponent value of another AFA alloy reported in [7]. At 600 °C, the  $n$  values of treated alloys decrease to 4.9 and 5.0 which are typical of  $n$  values for solid solution alloys [34].

The extrapolated threshold stresses of the treated alloys at 600 °C are much higher than those obtained at 700 °C. They decrease significantly with the increase in temperature of 100 °C. Three possible mechanisms are considered to explain the threshold stress in precipitation-strengthened alloys: (1) precipitate cutting, (2) Orowan dislocation bowing, (3) dislocation climbing [34].

The Orowan dislocation bowing stress for dislocation interact with  $\text{Ni}_3(\text{Al}, \text{Ti})$  particles is

Table 5

Threshold stresses extrapolated from  $\dot{\epsilon}^{1/5}$  vs  $\sigma$  plots.

Temperature (°C)	Threshold stress (MPa)		
	As-received DAFA29	TMT Method#1	TMT Method#2
600	–	670	574
700	217	50	9

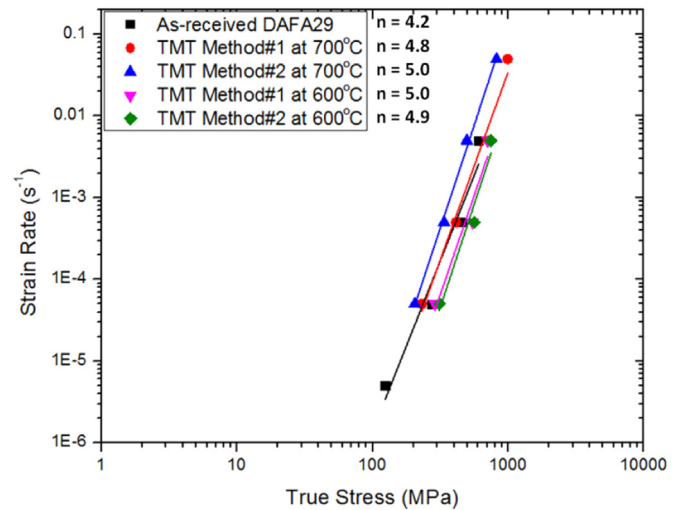


Fig. 10. Strain rate as a function of the effective stress ( $\sigma - \sigma_t$ ) for as-received and TMT DAFA29 alloys. The plots are on log-log scales.

$$\tau_o = \frac{Gb}{L-2r} \quad (7)$$

where  $\tau_o$  is the shear stress necessary for precipitates bypass by Orowan bowing,  $L$  is particle spacing,  $r$  is the radius of precipitates.

At 700 °C, the average size of  $\text{Ni}_3(\text{Al}, \text{Ti})$  precipitates is 35 nm after an 800 °C anneal for 2.4 h. The particle spacing obtained based on  $L$  and the volume fraction is 140 nm [15]. The volume fraction of  $\text{L}_{12}$  phase can be calculated based on density and phase fraction from a JMatPro simulation shown in Fig. 11.  $G$  is approximately 50 GPa for AFA alloys and  $b$  is estimate to be 0.253 nm. The calculated Orowan shear stress is about 180 MPa for both TMT AFA alloys. The threshold stress values of TMT alloys are about  $0.3\tau_o$  (50 MPa for Method#1) and  $0.05\tau_o$  (9 MPa for Method#2). These values are similar to those obtained from the Arzt-Ashby model for the local climb and general climb mechanisms [35]. For as-received DAFA29, the calculated Orowan shear stress is about 212 MPa with a particle spacing of 120 nm and average particle size of 30 nm. This Orowan stress is consistent with the threshold stresses of as-received DAFA29, which is 217 MPa.

At 600 °C, the threshold stress values are much higher than Orowan shear stress for both TMT alloys. This might be due to a

$\text{Ni-3.0Al-14.0Cr-45.44Fe-3.0Nb-0.15Si-2.0Ti-0.3Zr-0.01B-0.1C wt(\%)}$

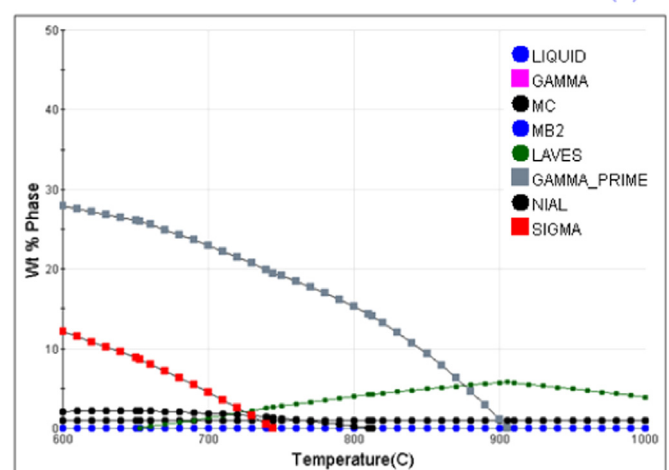


Fig. 11. Phase fractions of different phases in DAFA29 alloys from a JMatPro simulation.

change to a precipitate shearing mechanism and a higher volume fraction of  $\text{Ni}_3(\text{Al,Ti})$  at this temperature (Fig. 11).

#### 4.3. Dynamic strain aging of DAFA29

At 600 °C, the yield stress of as-received DAFA29 is insensitive to the strain rate, as shown in Fig. 5a. The flow stress curve shows evidence of negative strain rate sensitivity with significant serrated flow. This serrated flow starts when the strain rate jumps from  $5 \times 10^{-5}$  to  $5 \times 10^{-4} \text{ s}^{-1}$ . This phenomenon is also observed for other stainless steels and high temperature superalloys [36–40]. The serrated flow is expected to be associated with dynamic strain aging (DSA) which occurs at certain combinations of temperature and strain rate [36,40]. The occurrence of DSA is the result of solute diffusion in the metal lattice during plastic deformation at certain temperatures. The accumulation of these solute elements can impede the movement of dislocations and results in serrated flow curves. The solute elements typically responsible for this behavior are carbon below 550 °C, and Cr or Mo at temperatures above 550 °C [40,41].

#### 4.4. DAFA29 is insensitive to strain rate at 600 °C

The yield stress of DAFA29 is not dependent on the strain rate at 600 °C. This might be related to the work hardening of DAFA29 at this temperature. At 700 °C or higher, there is little work hardening for DAFA29 as shown in Figs. 1 and 2. The reduction of work hardening in as-received DAFA29 at temperature of 700 °C and higher temperature is due to a softening mechanism such as dynamic recovery which is expected to become the dominant mechanism at elevated temperature [38]. At higher temperatures, the work hardening due to the increase in dislocation density with increasing strain is counteracted by the formation of subgrains with low energy dislocations. Thermally-activated climb of dislocations is the prominent dynamic recovery mechanism for precipitate-strengthened alloys. This will overcome the obstacles of dislocation motion which is restrained at the lower temperature of 600 °C. This is also influenced by strain rate during tensile tests since the recovery is diffusion controlled process [38].

## 5. Conclusions

In this paper, the recently-developed AFA alloy, DAFA29, was treated by two TMT methods. The resulting fine-grained alloys were tensile tested at elevated temperature. Their mechanical properties were also evaluated by strain rate jump tests at two different temperatures. These results were compared to data for the as-received AFA alloy. The findings of this research are summarized as follows:

1. The TMT didn't increase the yield strengths of AFA alloys at 700 °C, although it significantly enhanced the yield strength of AFA alloys at room temperature.
2. The TMT AFA alloys have higher strain rate sensitivity and lower activation volume compared to as-received DAFA29 at elevated temperatures. The higher strain rate sensitivity and lower activation volume are due to the nanocrystalline grain size of the alloys.
3. For the two TMT AFA alloys, the strain rate and stress satisfy a power law relationship with the stress exponent around 5, whereas the stress exponent is around 4 for the as-received DAFA29. These values ruled out the mechanisms of bulk diffusion (Nabarro-Herring mechanism) and grain boundary diffusion (Coble mechanism) to explain the flow behavior.
4. At 700 °C, dislocation climb is the dominant mechanism for

deformation of TMT alloys. When the temperature decrease to 600 °C, the mechanism changes to dislocation shearing as indicated by the dramatically increased threshold stress.

5. The yield stress of TMT alloys decrease rapidly from 600 °C to 700 °C, which might be because increased diffusion rates in TMT alloys lead to fast dislocation climb at 700 °C. At this temperature, dislocation will be able to move around obstacles easily and the large volume of grain boundaries in TMT alloys work as sites of weakness.
6. The flow stress of the as-received AFA alloy is insensitive to strain rate at 600 °C due to strong work hardening at this temperature. It also shows significant serrated flow on the stress strain curve, which is associated with dynamic strain aging effect.

## Acknowledgments

This research was supported by the U.S. Department of Energy under NETL Award DEFG2612FE0008857. The authors would like to acknowledge Dr. Yukinori Yamamoto and Dr. Michael P. Brady of ORNL both for providing the AFA stainless steels and for their insightful advice.

## References

- [1] N. Evans, P. Maziasz, R. Swindeman, G. Smith, *Scr. Mater.* 51 (2004) 503–507.
- [2] R. Viswanathan, J. Henry, J. Tanzosh, G. Stanko, J. Shingledecker, B. Vitalis, R. Purgert, *J. Mater. Eng. Perform.* 14 (2005) 281–292.
- [3] P.D. Jablonski, J.A. Hawk, C.J. Cowen, P.J. Maziasz, *JOM* 64 (2012) 271–279.
- [4] Z. Zhong, Y. Gu, Y. Yuan, Z. Shi, *Met. Mat. Trans. A* 45 (2014) 343–350.
- [5] Y. Yamamoto, M.P. Brady, Z.P. Lu, P.J. Maziasz, C.T. Liu, B.A. Pint, K.L. More, H. Meyer, E.A. Payzant, *Science* 316 (2007) 433–436.
- [6] B.A. Pint, R. Peraldi, P. Maziasz, *Materials Science Forum*, Trans Tech Publ, Switzerland (2004), p. 815–822.
- [7] D. Zhou, X. Xu, H. Mao, Y. Yan, T. Nieh, Z. Lu, *Mater. Sci. Eng.: A* 594 (2014) 246–252.
- [8] M.P. Brady, J. Magee, Y. Yamamoto, D. Helmick, L. Wang, *Mater. Sci. Eng.: A* 590 (2014) 101–115.
- [9] M.P. Brady, Y. Yamamoto, M.L. Santella, P.J. Maziasz, B.A. Pint, C. Liu, Z. Lu, H. Bei, *JOM* 60 (2008) 12–18.
- [10] H. Bei, Y. Yamamoto, M.P. Brady, M.L. Santella, *Mater. Sci. Eng.: A* 527 (2010) 2079–2086.
- [11] Y. Yamamoto, M.P. Brady, M.L. Santella, H. Bei, P.J. Maziasz, B.A. Pint, *Met. Mat. Trans. A* 42 (2011) 922–931.
- [12] Y. Yamamoto, G. Muralidharan, M.P. Brady, *Scr. Mater.* 69 (2013) 816–819.
- [13] G. Trotter, I. Baker, *Mater. Sci. Eng.: A* 627 (2015) 270–273.
- [14] I. Tarigan, K. Kurata, N. Takata, T. Matsuo, M. Takeyama, in: *Proceedings of the MRS, Cambridge Univ Press*, 2011. mrsf10-1295-n1206-1203.
- [15] B. Hu, G. Trotter, I. Baker, M.K. Miller, L. Yao, S. Chen, Z. Cai, *Met. Mat. Trans. A* 46 (2015) 3773–3785.
- [16] R. Kozar, A. Suzuki, W. Milligan, J. Schirra, M. Savage, T. Pollock, *Met. Mat. Trans. A* 40 (2009) 1588–1603.
- [17] Z. Zhong, Y. Gu, Y. Yuan, T. Yokokawa, H. Harada, *Mater. Charact.* 67 (2012) 101–111.
- [18] K. Ma, H. Wen, T. Hu, T.D. Topping, D. Isheim, D.N. Seidman, E.J. Lavneria, J. M. Schoenung, *Acta Mater.* 62 (2014) 141–155.
- [19] M. Dao, L. Lu, R.J. Asaro, J.T.M. De Hosson, E. Ma, *Acta Mater.* 55 (2007) 4041–4065.
- [20] R.J. Asaro, S. Suresh, *Acta Mater.* 53 (2005) 3369–3382.
- [21] L. Capolungo, *Atomistic and Continuum Modeling of Nanocrystalline Materials: Deformation Mechanisms and Scale Transition*, Springer Science & Business Media, Germany, 2010.
- [22] S. Cheng, E. Ma, Y. Wang, L. Kecskes, K. Youssef, C. Koch, U. Trociewitz, K. Han, *Acta Mater.* 53 (2005) 1521–1533.
- [23] J. Chen, L. Lu, K. Lu, *Scr. Mater.* 54 (2006) 1913–1918.
- [24] F. Dalla Torre, P. Spätig, R. Schaublin, M. Victoria, *Acta Mater.* 53 (2005) 2337–2349.
- [25] Y.M. Wang, A.V. Hamza, E. Ma, *Acta Mater.* 54 (2006) 2715–2726.
- [26] Y. Wang, A. Hamza, E. Ma, *Appl. Phys. Lett.* 86 (2005) 241917.
- [27] J.K. Benz, L.J. Carroll, J.K. Wright, R.N. Wright, T.M. Lillo, *Met. Mat. Trans. A* 45 (2014) 3010–3022.
- [28] C. Allen, P. Delavignette, S. Amelinckx, *Phys. Status Solidi A* 9 (1972) 237–246.
- [29] A. Brown, M. Ashby, *Scr. Met.* 14 (1980) 1297–1302.
- [30] O.D. Sherby, P.M. Burke, *Prog. Mater. Sci.* 13 (1968) 323–390.
- [31] S. Zhu, S. Tjong, J. Lai, *Acta Mater.* 46 (1998) 2969–2976.

- [32] C. Stallybrass, A. Schneider, G. Sauthoff, *Intermetallics* 13 (2005) 1263–1268.  
 [33] R. Lagneborg, B. Bergman, *Met. Sci.* 10 (1976) 20–28.  
 [34] D.N. Seidman, E.A. Marquis, D.C. Dunand, *Acta Mater.* 50 (2002) 4021–4035.  
 [35] E. Arzt, M.F. Ashby, *Scripta Metallurgica*, 16 (1982) 1285–1290.  
 [36] A.K. Roy, J. Pal, C. Mukhopadhyay, *Mater. Sci. Eng.: A* 474 (2008) 363–370.  
 [37] W. Karlsen, M. Ivanchenko, U. Ehrnstén, Y. Yagodzinskyy, H. Hänninen, J. Nucl. Mater. 395 (2009) 156–161.  
 [38] K. Gopinath, A. Gogia, S. Kamat, R. Balamuralikrishnan, U. Ramamurty, *Met. Trans. A* 39 (2008) 2340–2350.  
 [39] J. Wright, J. Simpson, R. Wright, L. Carroll, T. Sham, in: *Proceedings of the ASME 2013 Pressure Vessels and Piping Conference*, American Society of Mechanical Engineers, 2013, pp. V01AT01A053–V001AT001A053.  
 [40] M. Hörnqvist, C. Joseph, C. Persson, J. Weidow, H. Lai, in: *Proceedings of the MATEC Web of Conferences*, EDP Sciences, 2014, pp. 16002.  
 [41] A. Nagesha, S. Goyal, M. Nandagopal, P. Parameswaran, R. Sandhya, M. Mathew, S.K. Mannan, *Mater. Sci. Eng.: A* 546 (2012) 34–39.